Journal Name

ARTICLE TYPE

Cite this: DOI: 10.1039/xxxxxxxxxx

Collective and convective effects compete in patterns of dissolving surface droplets

Gianluca Laghezza,[†a] Erik Dietrich,[†b,c] Julia M. Yeomans,[a] Rodrigo Ledesma-Aguilar, [d] E. Stefan Kooij, [b] Harold J. W. Zandvliet, [b] and Detlef Lohse[c,e]

Received Date
Accepted Date

DOI: 10.1039/xxxxxxxxxx

www.rsc.org/journalname

The effect of neighboring droplets on the dissolution of a sessile droplet, i.e. collective effects, are investigated both experimentally and numerically. On the experimental side small $20\ \mathrm{n}\ell$ approximately mono-disperse surface droplets arranged in an ordered pattern were dissolved and their size evolution is studied optically. The droplet dissolution time was studied for various droplet patterns. On the numerical side, Lattice-Boltzmann simulations were performed. Both simulations and experiments show that the dissolution time of a droplet placed in the center of a pattern can increase with as much as 60% as compared to a single, isolated droplet, due to the shielding effect of the neighboring droplets. However, the experiments also show that neighboring droplets enhance the buoyancy driven convective flow of the bulk, increasing the mass exchange and counteracting collective effects. We show that this enhanced convection can reduce the dissolution time of droplets at the edges of the pattern to values below that of a single, isolated droplet.

1 Introduction

The evaporation or dissolution of a single surface droplet is a well-studied topic due to its high importance in various applications, for example in the field of coating, and the deposition of particles[1–3]. Even more relevant but far less studied is the evaporation or dissolution of surface droplets surrounded by other droplets. This situation for example occurs whenever a spray is applied to a surface, or in inkjet printing. The presence of neighboring droplets makes the analytical approach more challenging as compared to a single droplet, and in general no analytical solution for the collective dissolution problem (on which we will focus here) exists. The addition of neighboring droplets, like in the pattern sketched in Fig. 1, is expected to change the concentration gradient by saturating the water in between the droplets, which in turn leads to a decrease in the mass loss rate. The mutual effect that neighboring droplets have on one another, referred to as the 'collective effect', has been studied in detail for spherical droplets inside sprays[4–7], due to its high relevance in for example spray cooling and fuel vaporization. In contrast to that, collective effects in the context of surface droplets are as of yet relatively unexplored. Available work describes one-dimensional diffusion above an infinite densely packed pattern where the effect of individual droplets is irrelevant[8,9], or only proposes the effect as the origin of delayed dissolution of polydisperse, randomly placed droplets. Only very recently, a first step was taken by Carrier et al[10] to asses the effect of a finite sized pattern of dissolving droplets, and compare the experimental results to a theoretical model. The latter work focussed on evaporation from an ordered pattern of ten droplets, or a random pattern of many polydisperse droplets. Moreover, an approximation was derived for the reduction in evaporating flux, based on the number and number density of the droplet, predicting reductions in the order of tens of percent's.

In this paper, we further investigate the collective effect in patterns of dissolving surface droplets. A diffuse interface numerical scheme is introduced and applied to simulate this system, and the numerical results are compared to experiments. Simulations and experiments on single droplets, finite, and infinite patterns are conducted. In particular, we will discuss the competition between on the one hand the slowed down dissolution due to the enhanced surrounding concentration thanks to the neighboring droplets and the resulting slower diffusion, and on the other hand enhanced convection due to collective convective effects.

---

[a] The Rudolf Peierls Centre for Theoretical Physics, 1 Keble Road, Oxford OX1 3NP, UK

[b] Physics of Interfaces and Nanomaterials,, MESA+ Institute for Nanotechnology, University of Twente, P.O. Box 217, 7500 AE Enschede, The Netherlands

[c] Physics of Fluids, MESA+ Institute for Nanotechnology and J. M. Burgers Centre for Fluid Dynamics, University of Twente, P.O. Box 217, 7500 AE Enschede, The Netherlands

[d] Department of Physics and Electrical Engineering, Northumbria University, Ellison Place, Newcastle upon Tyne NE1 8ST, UK

[e] Max Planck Institute for Dynamics and Self-Organization, 37077 Goettingen, Germany

† These authors contributed equally to this work.

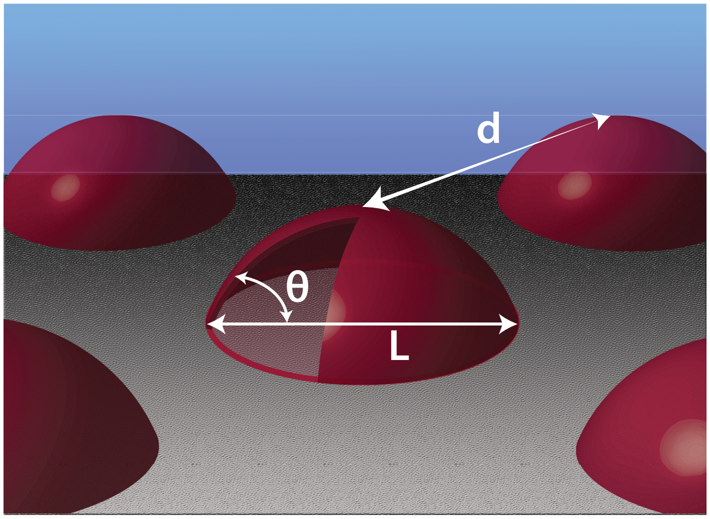

Fig. 1 (color online) Schematic drawing of a pattern of surface droplets with footprint diameter L and contact angle θ, placed in a hexagonal pattern with center-to-center distances d.

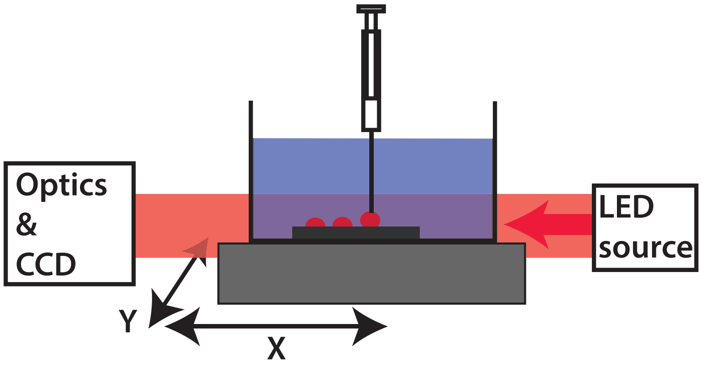

Fig. 2 (color online) Sketch (not to scale) of the experimental setup, showing the glass tank with the substrate placed under water. The syringe is connected to a syringe pump (not drawn) to dispense droplets of 1-heptanol. Using the X-Y translation stage, the tank is moved with respect to the syringe. A LED illuminates the middle droplet of the pattern, and projects the side view image of this droplet onto a long-distance microscope and CCD-camera.

2 Methods

2.1 Experimental procedure

A dissolving sessile droplet of long-chain alcohols in water is a versatile system to study various aspects of the dissolution process[11,12]. In the current work, 1-heptanol (Sigma-Aldrich, $\geq 98\%$ purity) is used: a long-chain alcohol with an oily appearance, which has a saturation solubility[13] $c_s = 1.67\ \mathrm{g\,L^{-1}}$ in water, a diffusion constant[14] $D = 0.8 \times 10^{-9}\ \mathrm{m^2\,s^{-1}}$, and a density[15] of $\rho_d = 819\ \mathrm{kg\,m^{-3}}$.

$2 \times 2\ \mathrm{cm^2}$ pieces of silicon wafers (P/Boron/(100), Okmetic), hydrophobized with PFDTS (1H,1H,2H,2H-Perfluorodecyltrichlorosilane 97%, ABCR GmbH, Karlsruhe Germany)[11] were used as substrates. These substrates were cleaned by insonication in acetone, and dried under a stream of nitrogen, prior to the experiment. The substrate was then placed at the bottom of a $5 \times 5 \times 5\ \mathrm{cm^3}$ glass tank, as sketched in Fig. 2. With the substrate in place, the cell was filled with 100 mL water, obtained from a millipore machine (Reference A+ system, Merck Millipore, at 18.2 MΩ cm). Subsequently, a glass-teflon syringe fitted with a thin needle (210 μm outer diameter) and connected to a motorized syringe pump, was put into the water. 20 nL ±4 nL droplets of the 1-heptanol were dispensed through the needle of the syringe and gently placed on the substrate. A motorized, computer controlled X-Y stage (Thorlabs) moved the cell and substrate with respect to the needle, and droplets were placed one by one to form patterns of $n = 5, 19, 41$, or 127 droplets, see for example Figs 3A-D. Droplets were placed in a hexagonal arrangement, as sketched in Fig. 1, with the exception of the outermost droplets in the largest pattern. All droplets in the experiments dissolved in the stick-jump mode[3,11,16], causing the contact angle θ of the droplet to vary between 65° and 70°. The time to create the largest pattern (127 droplets) was ≈ 15 minutes, which should be compared to the total dissolution time of > 2.5 hours. The relatively large volume of water in the tank ensured that even after complete dissolution of the largest pattern, the bulk saturation level was $\leq 0.02 c_s$.

A collimated light emitting diode light source (Thorlabs, $\lambda = 625$ nm) produced a beam parallel to the substrate and projected the side view image of the center droplet in the pattern onto a CCD camera (Pixelfly USB, PCO Germany) fitted with a long working distance microscope. Since other droplets would obscure the view of the center droplet, only this droplet was placed in the center row. The white arrow in Fig. 3 indicates the center droplet, and the direction of view. Simultaneous measurements of the outermost droplets were unfortunately impossible, as their side view was obscured by the surrounding droplets, prohibiting the accurate contact angle determination required for volumetric measurements. The images obtained were post-processed in Matlab to extract the profile with sub-pixel accuracy[17]. Other experiments were carried out as well to provide a top view of the droplet pattern. To this purpose, a droplet pattern was deposited in the usual way after which the tank was placed under a Leica DM2500H microscope, operated in the incident light mode, using a 5× magnification objective.

2.2 Numerical procedure

We performed three-dimensional simulations using a hydrodynamics model based on the Navier-Stokes equations and the Cahn-Hilliard model into which we have implemented evaporation following ref.[18]. The droplet-bulk system is considered as a binary liquid and by setting the chemical potential of the model at a value away from equilibrium, one phase is favored over the other. This physically corresponds to the situation that dissolution takes place if the solute concentration is lower than its saturation value (which is the equilibrium value). Three-dimensional surface droplets were simulated. For numerical optimization reasons we adopted a droplet contact angle of $\theta = 90°$. Note that this contact angle is different from the experiments, possibly leading to a difference in dissolving flux. However, as the current scope is

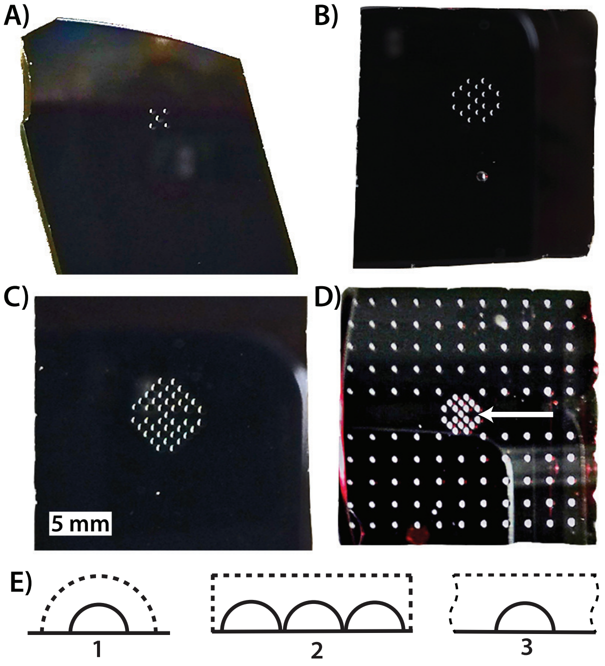

Fig. 3 (color online) A-D: Top view photographs of the water-immersed silicon substrate with the droplet patterns. The photographs show patterns with 5 (A), 19 (B), 41 (C), and 127 (D) 20 nL sized droplets of 1-heptanol. Panel E is a schematic side view of the numerical set-up showing the shell (E1), side (E2), top (E3) boundary condition used to simulate a single drop, multiple drops and an infinite array of drops respectively. The dashed lines in E indicate the surfaces, where the chemical potential is fixed at a non-equilibrium value to drive dissolution. The wavy dashed lines in Fig. (E3) represent periodic boundary conditions.

to identify the mechanisms in collective dissolution, rather than to obtain quantitative agreement between simulations and experiments, this difference is only qualitative. We adopted the following boundary conditions (see Fig. 3E):

1. For a single droplet, the chemical potential is fixed on a hemispherical shell surrounding the drop (referred to in the following as ”shell BC”);
2. For a finite pattern of droplets, the chemical potential is fixed at the top and the sides of the computational domain (”side BC”);
3. For an infinite pattern of droplets, the chemical potential is fixed at a plane at the top of the computational domain and periodic boundary conditions are applied at the sides of it (”top BC”).

More detailed information on the numerical procedure is provided in the appendix.

3 Results

3.1 Single droplet

To provide a simple test case and a basis to compare further measurements, we start with the dissolution of a single surface droplet, which has been well described in the context of the analogous processes of dissolving bubbles or evaporating droplets. In the case of steady-state, diffusion-limited dissolution, the dissolution rate of a droplet is given by[3,19–21],

$$\frac{dV}{dt} = -\frac{\pi L D (c_s - c_\infty)}{2\rho_d} f(\theta), \tag{1}$$

where,

$$f(\theta) = \frac{\sin\theta}{1+\cos\theta} + 4\int_0^\infty \frac{1+\cosh 2\theta\varepsilon}{\sinh 2\pi\varepsilon} \tanh[(\pi-\theta)\varepsilon]\mathrm{d}\varepsilon \tag{2}$$

is a geometrical factor to describe the effect of the droplet contact angle and the impermeable substrate. By inserting the values for a 1-heptanol droplet with initial volume $V_0 = 20$ nL, and numerical integration of Eq. (1), we obtain the black dashed line in Fig. 4 which represents the droplet volume as function of the time to dissolution $t-\tau$, where τ is the dissolution time: the time needed to completely dissolve the droplet.

Comparison of the experiments on single droplets of different initial volumes (plotted as the colored solid lines in Fig. 4) to the diffusion-limited model of a single droplet reveals a considerable discrepancy: the experiments are characterized by a higher rate of mass loss and therefore shorter dissolution time τ for a given initial volume. It has been shown[12] that the increased mass transport is caused by a convective contribution to the dissolution process, driven by solute-induced density gradients in the bulk.

The experimental results from Fig. 4 will be used in the next section, as they allow us to account for the variation in the initial droplet volumes: Despite the fact that great care is taken to create equally sized droplets, small differences in the initial droplet volume cannot be avoided. To allow for easy comparison between experiments with slight variations in the initial droplet volume, we correct for these deviations and compare the droplet volume to the desired initial volume of the droplets in the experiments (20 nL), namely by correcting the droplet volume V in each experiment according to

$$\tilde{V} = \frac{V}{V_0} \times 20\ \mathrm{n}\ell, \tag{3}$$

where $\tilde{V}$ is the corrected droplet volume (in nL), and V and V_0 are the volume and the initial volume of the droplet, respectively. The differences in the initial droplet volumes (even though only a few nl) significantly affect the total droplet dissolution time, thus obscuring the possible influence of collective effects. Therefore we must also correct the (dissolution) time based on the initial volume, which in diffusive problems is usually achieved by scaling with the appropriate time scale, namely the diffusive time scale $\tau_\mathrm{d} = R_0^2\rho/(\Delta c D)$, where R_0 is the initial droplet radius, and $\Delta c = c_s - c_\infty$. Scaling the time in such a way allows to compare purely diffusive droplet dissolution behavior, independent of the initial droplet size or the material[16,21]. Unfortunately, the diffusive time scale τ_d cannot be used in the current system as the mass transport is not purely diffusive. On the other hand, purely

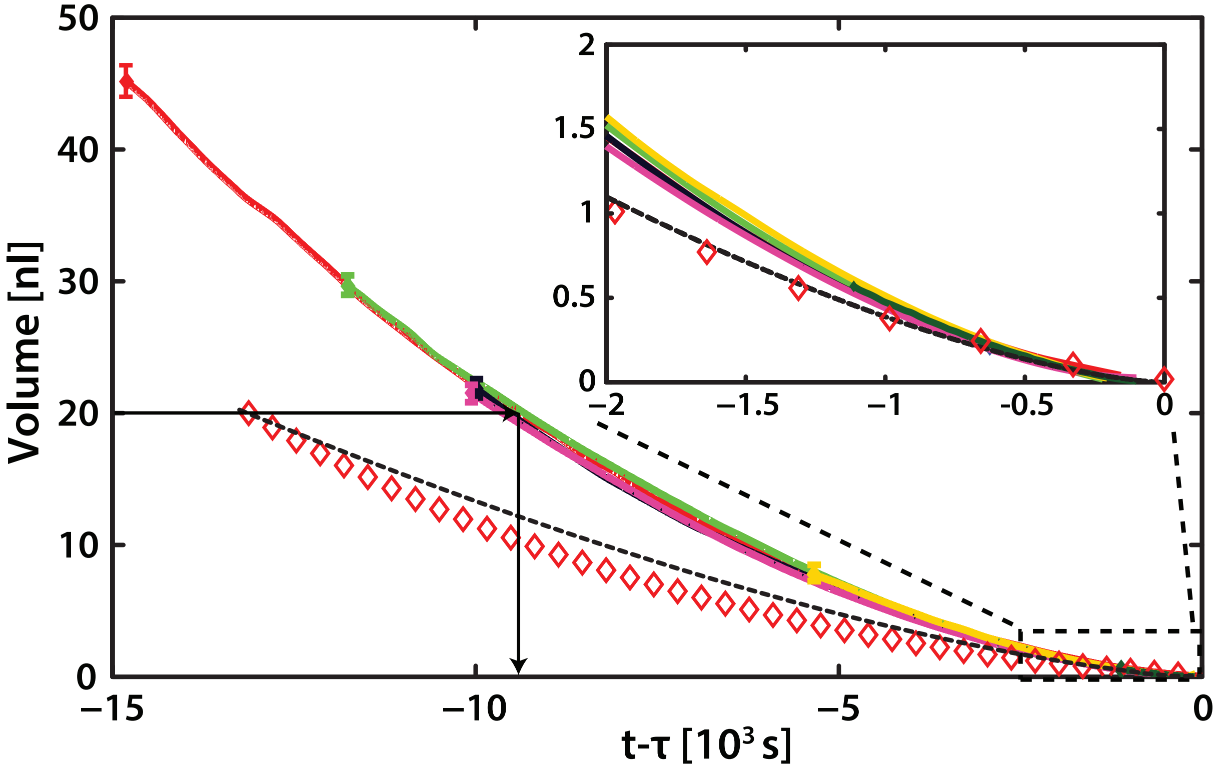

Fig. 4 (color online) Volume of single dissolving droplets as function of time until dissolution $t-\tau$. The black dashed line represents the expected diffusion-limited dissolution of a 20 nL 1-heptanol droplet (Eq. 1), to which the (purely diffusive) simulations (plotted as the open red diamonds) are compared. The experiments on individual droplets with of 1-heptanol and various initial volumes (solid lines of different colors) reveal an increased dissolution rate, due to a convective contribution to the dissolution[12]. We shift the x-axis by the droplet life time τ to overlap the individual measurements for comparison. The black arrows illustrate how the experiments can be used to find an empirical relation between the droplets initial volume and its dissolution time.

convective dissolution with the associated convective time scale[12]

$$\tau_c = \frac{4}{5a}\left(\frac{\nu\rho_d^4 R_0^5}{g\beta_c \Delta c^5 D^3}\right)^{1/4}. \quad (4)$$

where β_c is the bulk expansion coefficient, g the acceleration of gravity, and a a prefactor of order 1. Eq. (4) was shown to hold when the Rayleigh number

$$\mathrm{Ra} \equiv \frac{g\beta_c \Delta c R^3}{\nu D} > 12. \quad (5)$$

The Rayleigh number expresses the ratio of the buoyant force to the damping force, and for the current 1-heptanol droplets with volumes ≤ 20 nL, we find $0.5 < \mathrm{Ra} < 35$. This indicates droplet dissolution with contributions to mass transport from *both* convection and diffusion. This does neither allow for the use of the purely convective model, nor the purely diffusive model. Instead, both diffusion and convection play a role.

Therefore to proceed we exploit the single-droplet experiments to give an empirical relation between the initial volume of a single droplet and its dissolution time $\tau_{\mathrm{single}}(V_0)$. Using this relation, we correct time in each experiment according to

$$\tilde{t} = \frac{t}{\tau_{\mathrm{single}}(V_0)} \times 9100 \text{ s}, \quad (6)$$

where $\tilde{t}$ is the corrected time (in seconds), and $\tau_{\mathrm{single}}(V_0)$ is the dissolution time of a single, isolated droplet, based on the droplets' initial volume $16 \text{ nL} \leq V_0 \leq 24$ nL. $\tau_{\mathrm{single}}(V_0)$ is obtained from the single-droplet experiments, as illustrated by the black arrows in Fig. 4 for the case where $V_0 = 20$ nL. In Eq. (6), 9100 s represents the dissolution time of a single, isolated droplet with an initial volume of 20 nL, which is the desired initial droplet volume. [*]

To obtain a reference time scale for the simulations we map the simulation units to physical units by fixing the initial drop volume to 20 nL and then choose a time scale by matching the diffusive dissolution time scale $\pi LD(c_s - c_\infty)/2\rho_d$, the coefficient in Eq. (1), to its physical value. This corresponds to a dissolution time for a single drop of 13125 s. The scaled simulation results are shown as diamonds in Fig. 4. Deviations from the theoretical curve occur because of the difficulty of separating time scales i.e., transient effects: for simulations of a reasonable duration (in terms of CPU-time), the dissolution time is not sufficiently long compared to the diffusive time and the system is not exactly in

---

[*] Note that one cannot simply wait for a droplet with $V_0 > 20$ nL to dissolve down to $V = 20$ nL, as this would result in different waiting times, and with that variations in the volumes of the neighboring droplets.

diffusive equilibrium at all times[18].

The use of a time scale in seconds, rather than a dimensionless time is preferred as it emphasizes that the simulations and experiments are subject to different physical processes: purely diffusive dissolution in the simulations versus a combination of diffusive and convective dissolution in the experiments. Therefore this comparison must be interpreted as qualitative, and not quantitative. The absence of convection in the simulations is mainly due to the fact that the two phases have equal densities, so no buoyancy is present. Currently, steps are being taken to also incorporate convection into the simulations, which opens the way to achieving quantitative agreement between the simulations and the experiments.

3.2 Droplet patterns: shielding mechanism

It has been proposed[9] that the enhanced dissolution time for collective droplets is caused by a larger solute concentration in the (liquid) environment in between the droplets, due to their dissolving neighbors, thus reducing the concentration gradient and thus the mass transport. We confirm this by simulating a pattern with $n = 5$ droplets, and measuring the concentration along a diagonal cross-section through this pattern as shown in Figs. 5A and 5B. The solid colored lines, shown in panel A, represent five iso-concentration lines measured at $t_1 = 1900$ s along the cross-section indicated by the dashed line in Fig. 5B. They illustrate how the middle droplet primarily responds to a concentration gradient in the vertical direction, whereas the droplets at the perimeter of the pattern also experience a gradient in the lateral directions. This should result in a reduced mass loss rate for the center droplet, as compared to the outer ones, and thus a relatively faster dissolution of the outer droplets. This is indeed the case, as shown by the droplet cross-sections (plotted at subsequent times $t_1 = 1900$ s, $t_2 = 8500$ s, and $t_3 = 13200$ s by the black dashed lines in Fig. 5A), by the top view images of the droplets (panels B-D), as well as by the evolution of the droplet footprint diameters in time (panel E). The cross sections in panel A also show that in the absence of pinning, the outer droplets dissolve asymmetrically, due to the higher mass loss rate at their exposed sides, i.e. fully consistent with recent findings[22].

Comparable behavior is observed in experiments on patterns of droplets, as shown in Fig. 6. The droplets at the perimeter of the analyzed $n = 23$ pattern dissolve more quickly than the inner droplets. The outermost droplets (numbers 5 and 6) disappear first, followed by the droplets placed in the middle row (numbers 2, 3, and 4). The dissolution time of the center droplet (number 1) is extended by $\approx 20\%$ as compared to an equally sized, single droplet. However, it is surprising to see that the dissolution times of the outermost droplets (5 and 6) are in fact much *shorter* ($\tau < 9100$ s) as compared to a single droplet. In absence of an accurate measurement of the droplet height, one should keep in mind that the shorter dissolution time of the outermost droplets (< 8000 s) cannot be explained by a smaller-than-expected initial volume, which has a minimum of $V_0 = 16$ nl, corresponding to $\tau_{\text{single}}(16nl) = 8000$ s. Analogously, the longer dissolution time of the central droplet (> 10000 s) cannot be explained by an initial volume of 24 nl ($\tau_{\text{single}}(24nl) = 10000$ s). Hence, something else must be responsible for the accelerated dissolution of the outermost droplets. We interpret that this is most likely caused by the increased convection over this droplet pattern, caused by the larger amount of droplets, and hence the larger volume of (lighter) alcohol-saturated water. This stronger convection subjects the outermost droplets to an enhanced flow of clean water, increasing the dissolution rate and shortening the life time of the outermost droplets. Further inward in the pattern, the flow of water becomes progressively saturated by the dissolving droplets, reducing the dissolution rate from the innermost droplets and extending their dissolution time.

The initial footprints of the six droplets are indicated in red in panels A-C, illustrating that in contrast to the simulations, the droplet contact lines in the experiments are pinned by unavoidable local surface defects. This is especially visible for droplets 1 and 5, which are pinned to a point on their initial contact line throughout the entire dissolution process.

3.3 Droplet patterns: collective behavior

We now proceed by changing the number of droplets in the system and experimentally study the dissolution behavior in patterns of $n = 5, 19, 41$, and 127 droplets, placed at distances $d = 700$ μm ± 100 μm apart (see Fig. 1), such that $d/L_0 = 1.4 \pm 0.2$. The same spacing to diameter ratio is adopted in the simulations of patterns containing either 5, or an infinite number of droplets; shell boundary conditions (BC) are used for the single droplet, top BC for the infinite matrix and side BC for the 5 droplet matrix. As the camera used for these experiments (as discussed in section 2.1) could only produce a sharp image of a single droplet, the following sections discuss and present only the behavior of the center droplet in each pattern (as indicated in Fig. 3). The volumes of the center droplets are plotted as function of time in Figs. 7A and B for the experiments and simulations, respectively. Note that the tildes ($\tilde{V}$) and time ($\tilde{t}$) in Fig. 7A indicate the rescaled parameters, which are corrected for variations in initial droplet sizes between the measurements. V and t in Fig. 7B are obtained using the conversion factors, obtained as discussed in subsection 3.1. No rescaling was required in the simulations, as all droplets have exactly identical initial volumes. The dissolution of a single droplet is plotted as a reference in both figures and illustrates that the addition of extra droplets has a strong effect on the dissolution dynamics. More specifically, the slopes of the $V(t)$ curves (i.e., the volume loss rate) decreases upon the addition of more droplets, thus extending the droplet dissolution time.

To better appreciate the collective effect on the dissolution time, the experimentally and numerically measured dissolution times τ of the center droplets are plotted as function of $\log_{10}(n)$ in Fig. 8. The competition between the collective convective effect (increasing the dissolution rate and reducing the life time) and the collective diffusive effect (leading to an extended life time) is nicely visible in the experiments on small patterns ($n = 5, 19$): no significant increase of the life time as compared to a single droplet can be observed. In these small patterns, the effect of the convective flow is such that it counteract the shielding effect of the

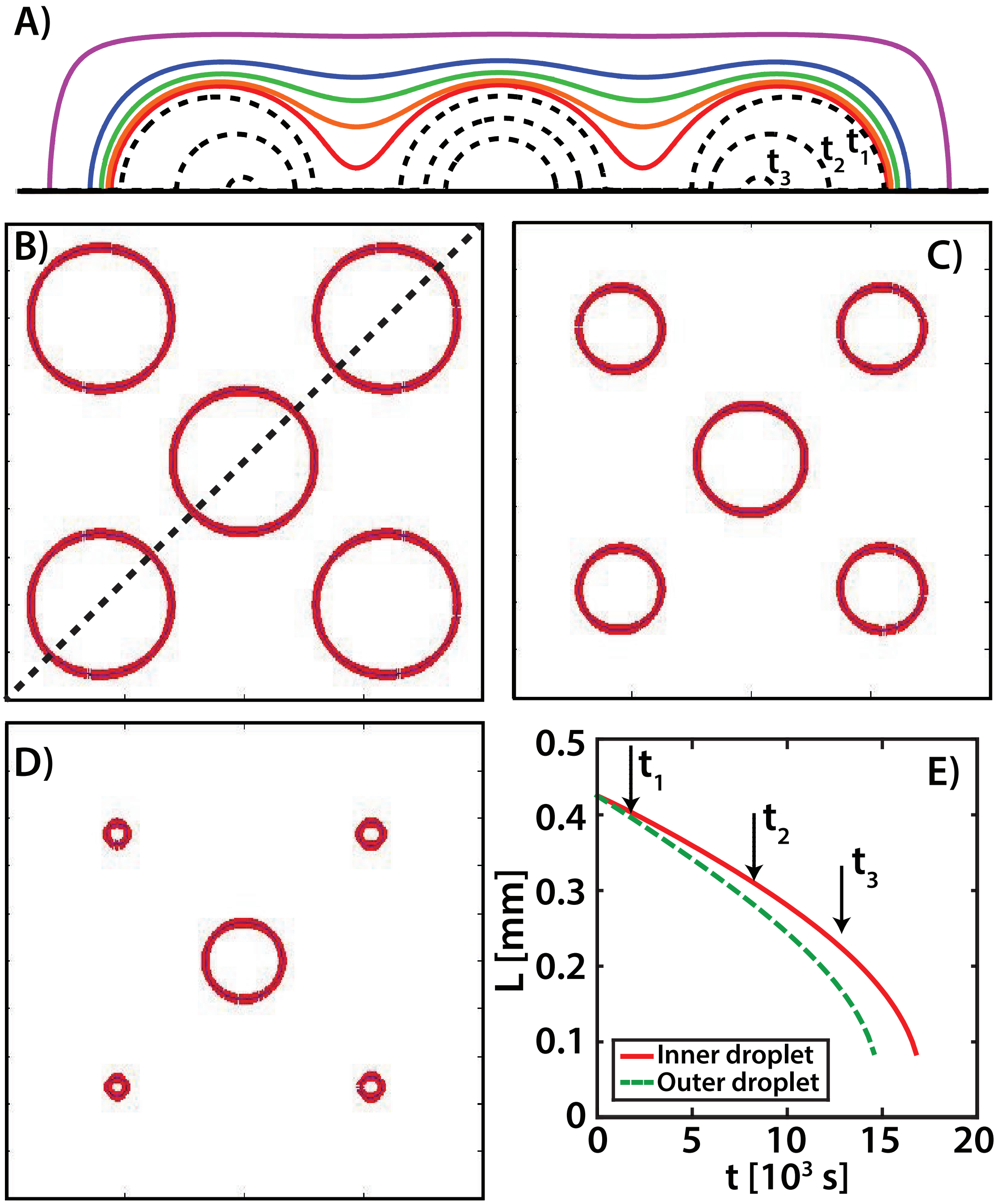

Fig. 5 (color online) A) The iso-concentration profiles (colored lines, measured at $t_1 = 1900$ s) show how the concentration in between the droplets is increased due to the neighboring droplets. The profile is measured diagonally through a pattern with $n = 5$ droplets, as indicated by the dashed line in panel B. The (dashed) contours of the droplets correspond to times $t_1 = 1900$ s (outermost contours), $t_2 = 8500$ s, and $t_3 = 13000$ s (innermost contours). Panels B-D show the droplet footprints at simulation times $t_1 = 1900$ s (B), $t_2 = 8500$ s (C), and $t_3 = 13200$ s (D). The footprint diameters L are plotted as function of time in (E); the evolution of L cannot be analysed for $L < 0.1$ due to the diffuse interface nature of the numerical model. The times at which panels B-D are taken are indicated by the black arrows in panel (E).

neighboring droplets. This shielding effect only becomes strong enough to counteract the effect of the collective convection in the larger patterns ($n = 41, 127$), where the dissolution time of the center droplet is extended significantly as compared to a single droplet ($\tau = 9100$ s). The effect of buoyancy driven convection is absent in the simulations, and hence a considerable increase of the droplet life time is already observed in the 5 droplet pattern.

3.4 Droplet patterns: effect of droplet spacing

So far, the droplets in all patterns, both in experiments and in numerics, were placed at a spacing to diameter ratio $d/L_0 = 1.4$. Still, for a given number of droplets in the experiments, the dissolution time of the center droplet is found to vary between experiments and we hypothesize that this is due to an unintentional variation in the positioning of the droplets, possibly resulting in

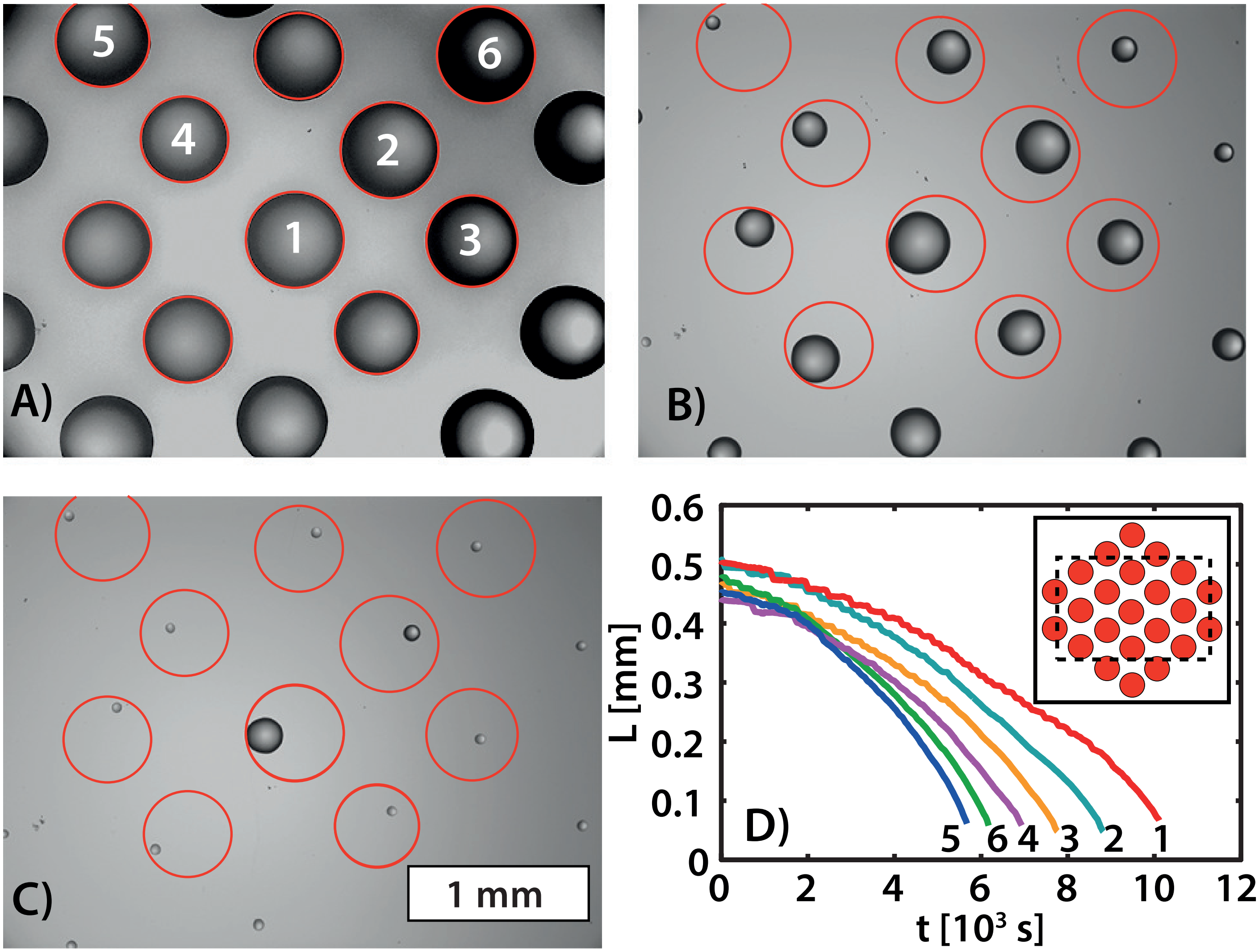

Fig. 6 (color online) Top view of a 23-droplet pattern ≈ 2 minutes after deposition (A), after 120 minutes (B), and after 170 minutes (C). The inset in (D) shows the original droplet pattern, the dashed box indicates the field of view. In (D) the footprint diameter is plotted as function of time, showing that the outer most droplets dissolve more quickly than the inner ones, and even more quickly than a single droplet ($\tau_{\mathrm{single}}(20\,\mathrm{n}\ell) = 9100$ s). The red circles outline the droplets original footprint, revealing that the droplets are pinned by surface defects, as their centers of mass move during the dissolution. The correction scheme for volume and time as described in section 3.1 (Eqs. (3) and (6)) has not been applied here, in order to show the raw data.

$d/L_0 \neq 1.4$. To test the influence of the (relative) droplet spacing on the dissolution process, we maintain the same droplet size ($V_0 = 20$ nL, $L_0 = 500$ μm), but construct patterns with different droplet spacing: the droplets were placed in a $n = 41$ pattern at ratios $d/L_0 = 1.1, 1.4, 2$, and 2.8 which we compared to simulations on infinite patterns with identical ratios d/L_0. Top boundary conditions were used in these simulations (Fig. 3, panel E3).

The resulting droplet volumes are plotted as function of time in Fig. 9, revealing that both in the experiments and in the simulations the dissolution time is considerably enhanced when the droplets are more densely packed. The dissolution time τ is plotted as function of d/L_0 in Fig. 10 for both the experiments and simulations for direct comparison. It should be noted that in the limit $d/L_0 \to \infty$ (i.e., a single droplet), the simulations are not expected to result into the same behavior as the single droplet treated in section 3.1, due to the different boundary conditions used.

4 Conclusion

A three-dimensional diffuse interface numerical scheme and experiments were used to study collective effects in patterns of dissolving droplets. A single droplet was used as a test case for comparison of the dissolution time of droplets placed at the center of finite and infinite patterns of mono-disperse droplets. For patterns comprising many droplets simulations and experiments were in good qualitative agreement, both measuring dissolution times of the center droplet typically tens of percent's longer than for a single droplet, with highest dissolution times measured for large, densely packed patterns.

Surprisingly, the experiments revealed a competition between an increased dissolution due to enhanced convection, and the inhibition of dissolution due to shielding by the neighboring drops. The influence of the convective flow was noticeable at the outermost droplets of the pattern, which exhibited dissolution times

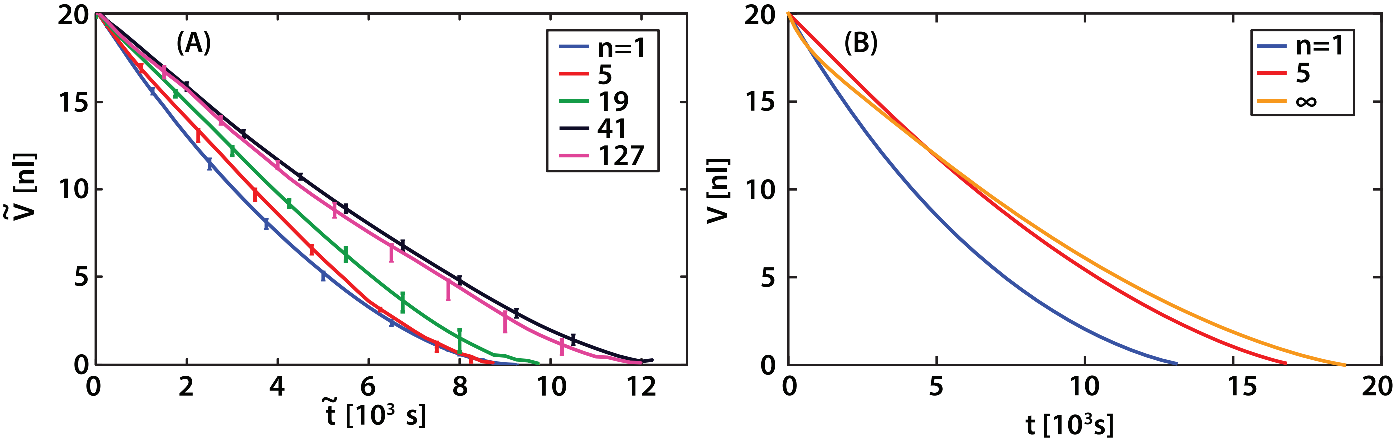

Fig. 7 (color online) Volume of the center droplet as function of time, as obtained from experiments (A) and numerics (B), for individual dissolving droplets and droplet patterns of various sizes. Volume and time in panel A have been rescaled (as described in section 3.1, see Eqs. (3) and (6)) to correct for small differences in the initial droplet volumes. Lines in (A) represent the mean of multiple experiments. The error bars indicate the spreading between different repetitions of the experiment.

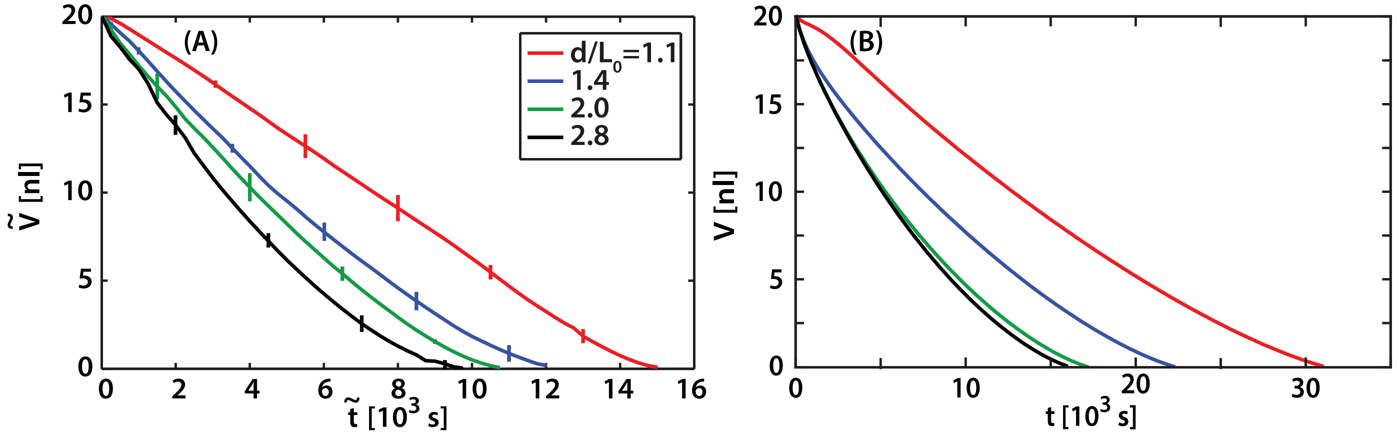

Fig. 9 (color online) Volume of the center droplet as function of time for experiments (A) and numerics (B) on patterns with different ratios between the droplet-droplet distance d and the initial droplet diameter L_0. Lines in (A) represent the mean of multiple experiments. The error bars indicate the spreading between different realizations of the experiments.

shorter as compared to an equally sized, single isolated droplet. Also for the center droplet in small ($n = 5, 19$) patterns, the enhanced convection was found to inhibit the shielding mechanism, leading to no clear increase in the dissolution time. Only for larger patterns of droplets, the collective effect was such that it counteracted the enhanced convection, and resulted in an extended dissolution time of the center droplet.

Our simulations confirmed the earlier hypothesis[9] that the reduced dissolution rate is caused by an increased concentration in between the droplets, lowering the concentration gradient and thus the dissolution rate. This effect was weaker at the edge of the pattern, causing the outermost droplets to dissolve more quickly than the inner droplets, an effect found in both the simulations and experiments.

Future numerical work should incorporate the effect of natural convection, or future experimental work could eliminate convection, for example by reducing droplet sizes, or conducting the dissolution experiments in a micro-gravity environment[23]. Also, the current experimental system was limited by the fact that it could only measure the center droplet of the pattern. Future work could be improved by simultaneous volumetric measurements of all droplets in the pattern, for example through top view imaging combined with interferometry to obtain height profiles of the dissolving droplets[24].

Acknowledgments

Andrea Prosperetti and Xuehua Zhang are gratefully acknowledged for continuing inspiring discussions. Maaike Rump and Kevin Hofhuis are acknowledged for assistance during the experiments.

Appendix: Numerical model

We describe the binary fluid by the Cahn-Hilliard free energy[25,26]

$$\mathscr{F} = \int_V \left(\mathscr{F}_b + \frac{\kappa}{2} |\nabla \phi|^2 \right) \mathrm{d}V + \int_S (h\phi_s) \mathrm{d}S \qquad (7)$$

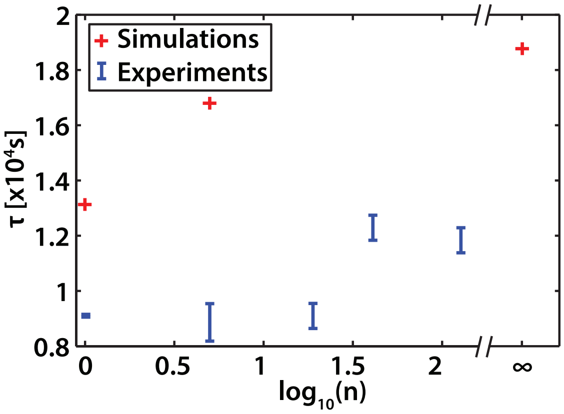

Fig. 8 (color online) Dissolution time τ of the center droplet vs $\log_{10}(n)$, where n is the number of droplets in the pattern. The experimental dissolution times are for the center droplet, and are corrected for variations of the initial volumes, as explained in subsection 3.1. Note that in the experiment the dissolution time for $n = 5$ droplets, is *smaller* than for a single one, due to convective effects.

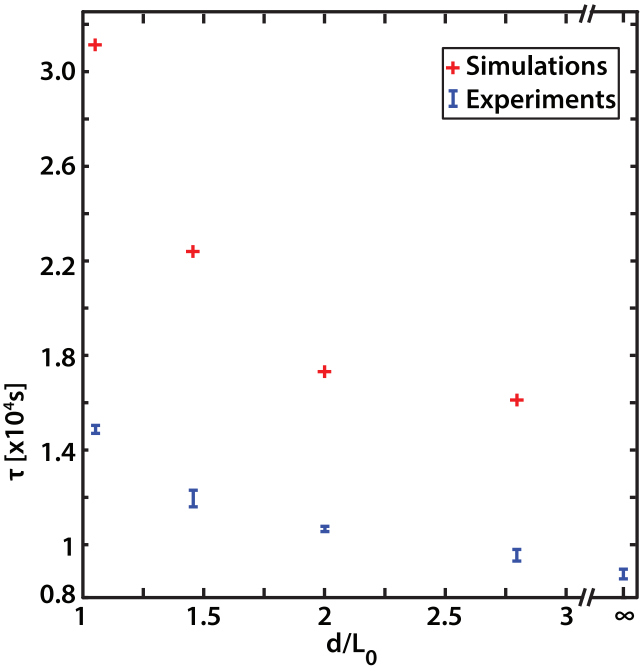

Fig. 10 (color online) Droplet dissolution time τ as function of the relative droplet spacing. Both experiments and simulations show that the droplet dissolution time is increased in a denser packing.

where

$$\mathscr{F}_b = \frac{\rho}{3}\log\rho + \frac{a}{2}\phi^2 + \frac{b}{4}\phi^4 \tag{8}$$

is the bulk free energy. The first term in the bulk free energy is an ideal gas term, ρ the density field and a and b model parameters. With this choice of the free energy, phase separation occurs if $a < 0$ and $b > 0$ and the ϕ field in each phase takes the values $\phi_b = \pm\sqrt{-a/b}$. The second term in Eq. (7) represents the surface tension, which takes the value $\gamma = \sqrt{-8ka^3/9b^2}$. This is a diffuse interface model and the interface width is $\varepsilon = \sqrt{-2\kappa/a}$; it can be shown that near an interface ϕ varies according to

$$\phi(r) = \phi_b \tanh\frac{r}{\varepsilon} \tag{9}$$

where r is the normal coordinate to the interface.

In the limit of negligible convection the concentration field evolves following to the diffusion equation

$$\frac{\partial\phi}{\partial t} = M\nabla^2\mu, \tag{10}$$

where M is the mobility and the chemical potential

$$\mu \equiv \frac{\delta\mathscr{F}}{\delta\phi} = a\phi + b\phi^3 - \kappa\nabla^2\phi. \tag{11}$$

We solve Eq (10) using a Lattice-Boltzmann algorithm.

In the LB algorithm, both space and velocity are discretized[27]. We discretize space by using a cubic lattice of spacing $\Delta x = 1$, and the D3Q15 lattice is used to discretize the velocities: D3 refers to three spatial dimensions and Q15 to 15 velocities (for more details see[27]). The probability distribution functions $f(r,v,t)$ used in the Boltzmann equation now becomes $f_i(r,t)$ because we have only discrete velocities (the i index refers to the discrete set of velocities used). Since we have two fluids, we need two distribution functions, f_i and g_i. The evolution of the distribution functions is given by a discretization of the Bhatnagar-Gross-Krook (BGK) approximation[28] of the Boltzmann equation

$$f_i(r + e_i\Delta t, t + \Delta t) - f_i(r,t) = -\frac{\Delta t}{\tau_f}(f_i - f_i^{eq}) \tag{12a}$$

$$g_i(r + e_i\Delta t, t + \Delta t) - g_i(r,t) = -\frac{\Delta t}{\tau_g}(g_i - g_i^{eq}). \tag{12b}$$

where we chose time steps $\Delta t = 1$ and e_i is the vector of the discrete velocities used. The algorithm can be split in two steps: the collision step (corresponding to the right hand side of the previous equations), where the distribution functions relax towards their equilibrium values with timescales τ_f and τ_g, and the propagation step (left hand side of the equations), where they move to their neighbor sites. Hydrodynamic fields (density ρ, velocity v, pressure P, etc.) are defined by

$$\rho = \sum_i f_i \qquad \rho v_\alpha = \sum_i e_{i\alpha} f_i$$

$$P_{\alpha\beta} + \rho v_\alpha v_\beta = \sum_i f_i e_{i\alpha} e_{i\beta} \tag{13}$$

$$\sum_i g_i = \phi \qquad \sum_i g_i e_{i\alpha} e_{i\beta} = \hat{M}\mu\delta_{\alpha\beta} + \phi v_\alpha v_\beta \tag{14}$$

where the indices α and β indicate the spatial components of vectors and tensors, and $\hat{M}$ is a parameter related to the mobility M. Mass and momentum conservation are satisfied by enforcing the f_i^{eq} and g_i^{eq} to satisfy the same eqs. 13-14 of their non-equilibrium counterparts and to be consistent with both the stress tensor and the thermodynamics of the model. It is customary to expand the equilibrium distribution function at second order in velocity

$$f_i^{eq}(r,t) = A_\sigma + B_\sigma e_{i\alpha} v_\alpha + C_\sigma v^2 + D_\sigma (e_{i\alpha} v_\alpha)^2 \qquad (15)$$

and analogously for g_i. The coefficients A, B, C, D are chosen in order to satisfy the hydrodynamic equations and the previous constraints. The hydrodynamic equations can be recovered from Eq. 12 by a Chapman-Enskog expansion[29,30]. The transport coefficients are found to be linked with the LB relaxation times by

$$\eta = \frac{2\tau_f - 1}{6} \qquad M = \frac{\tau_g - 1}{2}\hat{M}. \qquad (16)$$

The parameters used are $-a = b = 0.00305$, $\kappa = 0.0078$ and $M = 5$ and $\rho = 1$. The simulation domain was of size $(N_x, N_y, N_z) = (100, 100, 50)$ for the single drop and infinite pattern case, and $(N_x, N_y, N_z) = (200, 200, 50)$ for the five droplet pattern. Unless stated otherwise, the initial footprint diameter of the drop was $L_0 = 60$. This choice of parameters has already been validated in[18].

The chemical potential is fixed at the boundaries as described in section 2.2 by fixing the order parameter ϕ and using Eq. 11. Details are given in ref.[18].

References

1 A.-M. Cazabat and G. Guena, *Soft Matter*, 2010, **6**, 2591–2612.

2 H. Y. Erbil, *Adv. Colloid Interface Sci.*, 2012, **170**, 67–86.

3 D. Lohse and X. Zhang, *Rev. Mod. Phys.*, 2015, **87**, 981–1035.

4 S. K. Aggarwal and F. Peng, *J. Eng. Gas Turb. Power*, 1995, **117**, 453–461.

5 T. Kalwarczyk, N. Ziebacz, M. Fiałkowski and R. Hołyst, *Langmuir*, 2008, **24**, 6433–6440.

6 P. S. Sánchez, *Ph.D. thesis*, Institut National Polytechnique de Toulouse, 2012.

7 M. Rohloff, T. Lapp and J. Vollmer, *arXiv:1411.7882v1*, 2014.

8 J. H. Weijs, J. R. T. Seddon and D. Lohse, *ChemPhysChem*, 2012, **13**, 2197–2204.

9 J. H. Weijs and D. Lohse, *Phys. Rev. Lett.*, 2013, **110**, 054501.

10 O. Carrier, N. Shahidzadeh-Bonn, R. Zargar, M. Aytouna, M. Habibi, J. Eggers and D. Bonn, `www.maths.bris.ac.uk/majge/evaporationwater_v32012.03.40.pdf` accessed April 2016.

11 E. Dietrich, E. S. Kooij, X. Zhang, H. J. W. Zandvliet and D. Lohse, *Langmuir*, 2015, **31**, 4696–4703.

12 E. Dietrich, S. Wildeman, C. W. Visser, K. Hofhuis, E. S. Kooij, H. J. W. Zandvliet and D. Lohse, *accepted for publication in J. Fluid Mech.*, 2016, **(in press)**, year.

13 K. Kinoshita, H. Ishikawa and K. Shinoda, *Bulletin of the Chemical Society of Japan*, 1958, **31**, 1081–1082.

14 L. Hao and D. G. Leaist, *J. Chem. Eng. Data*, 1996, **41**, 210–213.

15 M. A. Rauf, G. H. Stewart and Farhataziz, *Journal of Chemical & Engineering Data*, 1983, **28**, 324–328.

16 X. Zhang, J. Wang, L. Bao, E. Dietrich, R. C. A. van der Veen, S. Peng, J. Friend, H. J. W. Zandvliet, L. Yeo and D. Lohse, *Soft Matter*, 2015, **11**, 1889–1900.

17 A. van der Bos, M.-J. van der Meulen, T. Driessen, M. van den Berg, H. Reinten, H. Wijshoff, M. Versluis and D. Lohse, *Phys. Rev. Applied*, 2014, **1**, 014004.

18 R. Ledesma-Aguilar, D. Vella and J. M. Yeomans, *Soft Matter*, 2014, **10**, 8267–8275.

19 R. Picknett and R. Bexon, *Journal of Colloid and Interface Science*, 1977, **61**, 336 – 350.

20 Y. O. Popov, *Phys. Rev. E*, 2005, **71**, 036313.

21 H. Gelderblom, A. G. Marín, H. Nair, A. van Houselt, L. Lefferts, J. H. Snoeijer and D. Lohse, *Phys. Rev. E*, 2011, **83**, 026306.

22 A. J. D. Shaikeea and S. Basu, *Langmuir*, 2016, **32**, 1309–1318.

23 F. Carle, S. Semenov, M. Medale and D. Brutin, *International Journal of Thermal Sciences*, 2016, **101**, 35 – 47.

24 R. C. A. van der Veen, T. Tran, D. Lohse and C. Sun, *Phys. Rev. E*, 2012, **85**, 026315.

25 A. Bray, *Advances in Physics*, 1994, **43**, 357–459.

26 H. Kusumaatmaja and J. M. Yeomans, in *Simulating Complex Systems by Cellular Automata*, Springer Berlin Heidelberg, 2010, pp. 241–274.

27 J.-C. Desplat, I. Pagonabarraga and P. Bladon, *Computer Physics Communications*, 2001, **134**, 273 – 290.

28 P. L. Bhatnagar, E. P. Gross and M. Krook, *Phys. Rev.*, 1954, **94**, 511–525.

29 J. Yeomans, *Physica A: Statistical Mechanics and its Applications*, 2006, **369**, 159 – 184.

30 S. Succi, *The Lattice Boltzmann Equation: For Fluid Dynamics and Beyond*, Oxford university press, 2013.